Supplementary Information

Structural reconfiguration of interacting multi-particle systems through parametric pumping

Qinghao Mao[1,2,*], Brady Wu[1,2], Bryan VanSaders[2], and Heinrich M. Jaeger[1,2]

[1]Department of Physics, University of Chicago, 929 E 57th St, Chicago, IL 60637, USA

[2]James Franck Institute, University of Chicago, 929 E 57th St, Chicago, IL 60637, USA

[*]Corresponding author. Email: qinghaomao@uchicago.edu

Effective modulation depth $\varepsilon_{\mathbf{am}}^{\mathbf{eff}}$

When the input signal to the transducer is modulated according to $V = V_0 \sin(2\pi f t)(1 + \varepsilon_{\mathrm{am}} \sin(2\pi f_{\mathrm{am}} t))$, we can rewrite it as

$$\begin{aligned} V &= V_0 \left(\sin(2\pi f t) + \varepsilon_{\mathrm{am}} \sin(2\pi f t) \sin(2\pi f_{\mathrm{am}} t)\right) \\ &= V_0 \left(\sin(2\pi f t) - \frac{1}{2}\varepsilon_{\mathrm{am}} \cos(2\pi (f + f_{\mathrm{am}})) + \frac{1}{2}\varepsilon_{\mathrm{am}} \cos(2\pi (f - f_{\mathrm{am}}) t)\right) \\ &= V_0 \sin(2\pi f t) - \frac{1}{2}\varepsilon_{\mathrm{am}} V_0 \cos(2\pi (f + f_{\mathrm{am}}) t) + \frac{1}{2}\varepsilon_{\mathrm{am}} V_0 \cos(2\pi (f - f_{\mathrm{am}}) t) \end{aligned} \tag{S1}$$

Therefore, driving the transducer with this modulated signal is equivalent to the superposition of three separate signals with frequencies f, $f + f_{\mathrm{am}}$ and $f - f_{\mathrm{am}}$, and strengths V_0, $\frac{1}{2}\varepsilon_{\mathrm{am}} V_0$ and $\frac{1}{2}\varepsilon_{\mathrm{am}} V_0$. Since the acoustic cavity has a frequency-dependent response, the sound pressure will be

$$\begin{aligned} p_{\mathrm{ac}} =& \xi_f V_0 \sin(2\pi f t) \\ &- \xi_{f+f_{\mathrm{am}}} \frac{1}{2}\varepsilon_{\mathrm{am}} V_0 \cos(2\pi (f + f_{\mathrm{am}}) t) \\ &+ \xi_{f-f_{\mathrm{am}}} \frac{1}{2}\varepsilon_{\mathrm{am}} V_0 \cos(2\pi (f - f_{\mathrm{am}}) t), \end{aligned} \tag{S2}$$

where ξ_f is the pressure response function of the acoustic cavity when driven with frequency f. Setting

$$\begin{aligned}\xi_+ &= \frac{1}{2}(\xi_{f+f_{am}} + \xi_{f-f_{am}}),\\ \xi_- &= \frac{1}{2}(\xi_{f+f_{am}} - \xi_{f-f_{am}}),\end{aligned} \tag{S3}$$

the pressure p_{ac} becomes

$$\begin{aligned}p_{\mathrm{ac}} =&\xi_f V_0 \sin(2\pi f t)\\ &-\frac{1}{2}(\xi_+ + \xi_-)\varepsilon_{\mathrm{am}} V_0 \cos(2\pi(f + f_{\mathrm{am}})t)\\ &+\frac{1}{2}(\xi_+ - \xi_-)\varepsilon_{\mathrm{am}} V_0 \cos(2\pi(f - f_{\mathrm{am}})t)\\ =&\xi_f V_0 \sin(2\pi f t)\\ &+\frac{1}{2}\xi_+\varepsilon_{\mathrm{am}} V_0(-\cos(2\pi(f + f_{\mathrm{am}})t) + \cos(2\pi(f - f_{\mathrm{am}})t))\\ &-\frac{1}{2}\xi_-\varepsilon_{\mathrm{am}} V_0(\cos(2\pi(f + f_{\mathrm{am}})t) + \cos(2\pi(f - f_{\mathrm{am}})t)).\end{aligned} \tag{S4}$$

Thus,

$$\begin{aligned}p_{\mathrm{ac}} =&\xi_f V_0 \sin(2\pi f t)\\ &+\xi_+\varepsilon_{\mathrm{am}} V_0 \sin(2\pi f t)\sin(2\pi f_{\mathrm{am}} t)\\ &-\xi_-\varepsilon_{\mathrm{am}} V_0 \cos(2\pi f t)\cos(2\pi f_{\mathrm{am}} t).\end{aligned} \tag{S5}$$

If the response function of the horn is symmetric in modulation frequency, i.e., $\xi_{f+f_{am}} = \xi_{f-f_{am}} = \xi_+$, and therefore $\xi_- = 0$, the effective modulation depth is

$$\varepsilon_{\mathrm{am}}^{\mathrm{eff}} = \frac{\xi_+}{\xi_f}\varepsilon_{\mathrm{am}}. \tag{S6}$$

This effective depth is smaller than $\varepsilon_{\mathrm{am}}$ because $\xi_+ < \xi_f$, and it will decrease monotonically as f_{am} grows (see Fig. 2e, red trace; Fig. 3d, black trace). However, such symmetry is not preserved when the acoustic cavity is driven at frequencies away from its resonance, $f \neq f_{\mathrm{res}}$. In this case, we cannot ignore contributions from ξ_-, which can be a non-monotonic function of f_{am}. Therefore, a non-monotonic response as a function of f_{am} can be expected (see Fig. 2e, pink trace).

Out-of-plane modes of the levitated 2-particle system

The 2-sphere system has two additional, out-of-plane VMs. The rocking mode, in which the vertical motions of the particles are out of phase, has a frequency very close to the in-plane mode, and experimentally we treat both as one single, degenerate mode, Supplementary Fig. 1. However, the vertical vibrational mode, in which both particles move up and down together, has a much lower eigenfrequency (smaller than 40Hz) so that the regions of resonance where this mode can be activated do not appear in the pumping state diagram in Fig. 2e.

Ability to control larger systems

The 13-sphere cluster enables us to test the performance of the parametric pump-quench method in systems with a high-dimensional configuration space, where we can easily adjust the particle number and the damping coefficient. The LJ simulation is carried out with LAMMPS at zero temperature and the interaction is given by the standard LJ potential

$$E = 4\epsilon \left[(\frac{\sigma}{r})^{12} - (\frac{\sigma}{r})^{6} \right], \tag{S7}$$

with $\epsilon = 1$ and $\sigma = 1$ and a cutoff distance $r_c = 5$. A weak confining force is applied to all particles to keep them sufficiently close to each other during the pumping period and removed during the quenching period to avoid its bias on base energy.

To demonstrate the possibility of selecting a more complicated state, we extended the analysis by applying the pump-quench method to control another structure in the LJ system (Supplementary Figure 5). Its state diagram exhibits greater overlap with others, making it more challenging to select. To achieve this target state, we use two frequencies, i.e., the method discussed in the main text with the rod-and-two-spheres system. These frequencies are marked by blue crosses in Supplementary Figure 5a. We apply one pump at its small peak at $f_{am} = 5.5$ to destabilize other structures and another pump at $f_{am} = 7.4$, targeting the icosahedron. With these two frequencies, the probability of staying outside the target state decays more slowly than the state shown in Fig. 4d, 50% after 200 cycles, but it still follows an exponential decay. This aligns with our understanding of state selection as a Markov process and suggests that, as long as the states' diagrams are not completely overlapping, biasing and hence control is still possible.

Supplementary Figure 6a, b gives an example of the pumping state diagrams of two different structures with $N = 13$. When we compare the two pumping state diagrams, γ_r^* and γ_b^*, the relative growth rate for the red and the blue structure (Supplementary Fig. 6c), one of the states will always have a higher VM frequency than the other. Without a restriction on $\varepsilon_{\mathrm{am}}$ as a function of f_{am}, the higher-frequency mode can always be selectively excited. However, in experiment $\varepsilon_{\mathrm{am}}$ is capped from above ($\varepsilon_{\mathrm{am}}^{\mathrm{eff}}$).

In simulations, we mimic this feature of experiments and manually apply a restriction on the largest $\varepsilon_{\mathrm{am}}$ available for each f_{am}, i.e., an $\varepsilon_{\mathrm{am}}^{\mathrm{eff}}$ curve. Here we use an experimentally plausible curve (a Gaussian function with a half height at $f_{\mathrm{am}} = 6\mathrm{Hz}$), shown by the black line. With that, the available parameters to activate one structure but not activate the other one are highlighted as the bright regions in Supplementary Fig. 6d, e, separately. One-way control becomes possible if one can find a bright region in one of these plots, and two-way control becomes possible if bright regions are found in both of them.

We now vary the number of particles N to check the controllability as a function of N. For each N we randomly generate 100 initial conditions by collapse of a randomized cloud at zero temperature. The number of energetically unique structures found within these 100 cases increases with N until $N \simeq 25$, at which point the configuration space of the cluster is too large to be accurately sampled with 100 trials (Supplementary Fig. 7a). We then compare all pairs among the unique structures and calculate the possibility of one-way and two-way control between them, see Supplementary Fig. 7b. To do this, a threshold on the growth rate γ^* is chosen to be 1.1, 1.5, or 2.0, as the growth rate has to be slightly larger than the damping rate to overcome nonlinear effects present for finite amplitude oscillations. In these simulations, we vary the damping coefficient, and we define a relative damping coefficient $\gamma_d^* = \frac{\gamma_d}{\gamma_{d,13}}$, where $\gamma_{d,13}$ is the one used in the 13-particle LJ example discussed in the main text. Thus, $\gamma_d^* = 1.0$ represents the case shown in Fig. 4c, d. From Supplementary Fig. 7b, we find that P(one-way) and P(two-way) behave qualitatively similarly: the controllability depends strongly on γ_d^* when the threshold of γ^* is set large enough, indicating that only in a sufficiently underdamped system is parametric pumping strong enough to break a structure apart. This controllability decreases rapidly as N increases when γ_d^* is large, but controllability can be maintained at a high level when γ_d^* is small. Interestingly, a peak in controllability is observed around $N = 13$, where many structures are close to the icosahedral structure that has a high degree of symmetry.

This creates characteristic gaps in the parametric pumping diagram, as shown in Fig. 4c, and it promotes controllability with parameters that target these gaps.

Though the controllability between a pair of structures in the LJ system decreases for larger particle number N, and it becomes more difficult if the interaction is highly non-linear, a lower damping coefficient γ_d^* and a higher symmetry in the targeted structure can greatly enhance the chance of finding appropriate control parameters in the pumping state diagram. This demonstrates the benefit of using techniques like acoustic levitation in air, where the damping coefficient is much lower than in a liquid.

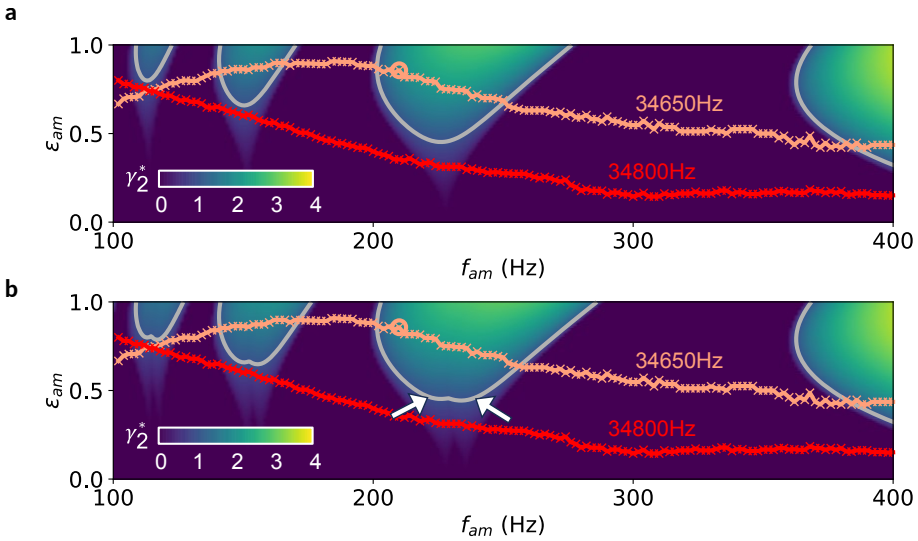

Supplementary Figure 1: Rocking mode pumping state diagram for the 2-particle 'molecule'. **a**, Growth rate of the in-plane vibration mode. Data are the same as Fig. 2e. **b**, Maximum growth rate of the 2-particle 'molecule' vibration modes, including both the in-plane breathing mode and the out-of-plane rocking mode. With the rocking mode taken into consideration, isolines (gray) are nearly identical to those of the in-plane breathing mode, except for a slight widening of the peaks and tiny variations in the shape, for example in the region book-ended by the white arrows. Experimentally the two modes therefore are treated as one degenerate mode.

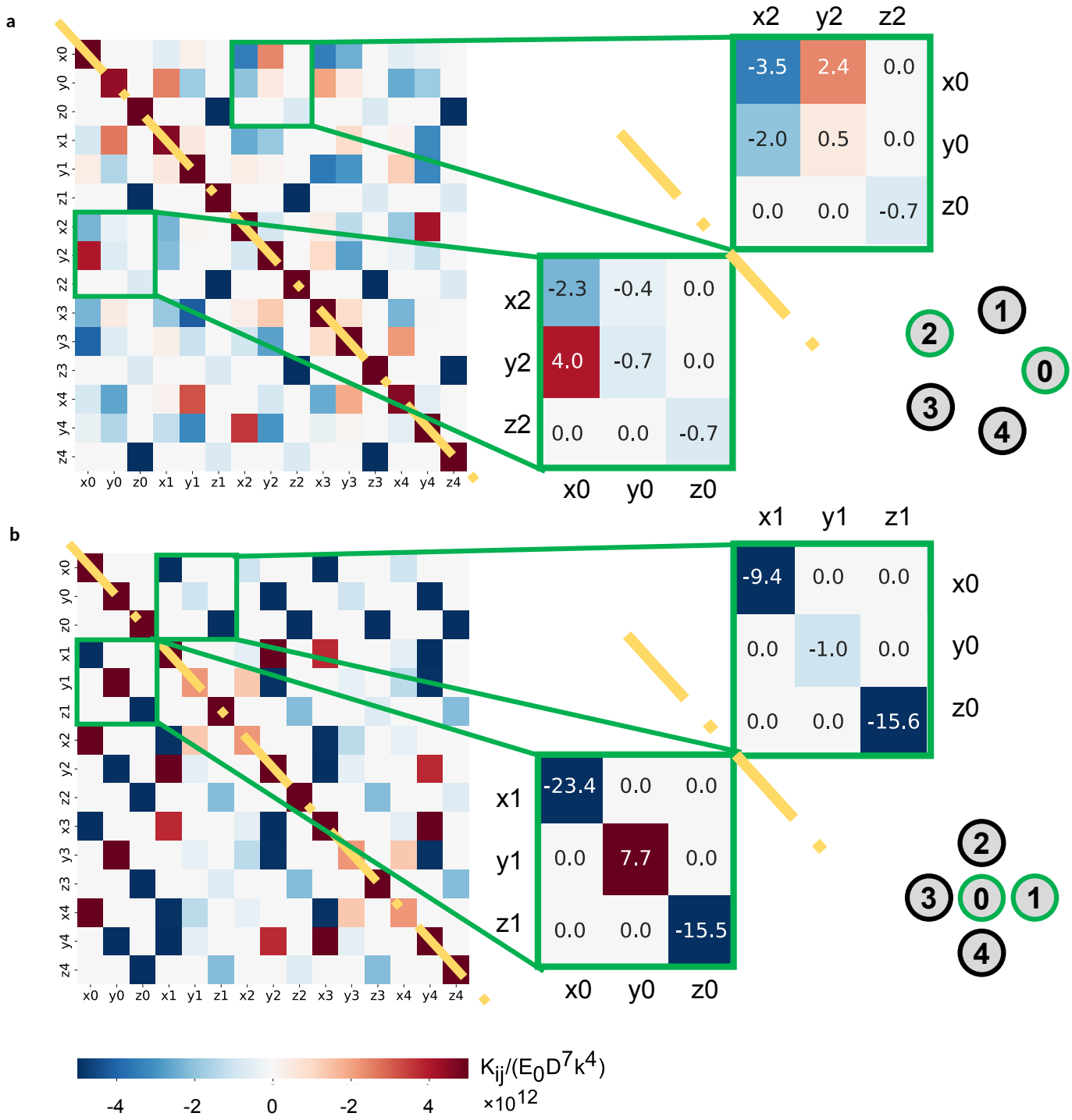

Supplementary Figure 2: Stiffness matrix K for the two states of the 5-particle cluster. **a**, Pentagon state. **b**, Cross state. In both panels, the stiffness matrix contains entries that correspond to the slope of the linear response when particles are displaced slightly in xyz-direction from their stable position and thereby generate forces on the other particles. For each stiffness matrix two zoomed-in views highlight representative blocks on either side of the diagonal, demonstrating the asymmetry of interactions between particles. Lower right corners: Labeling of the five particles in the stable configurations.

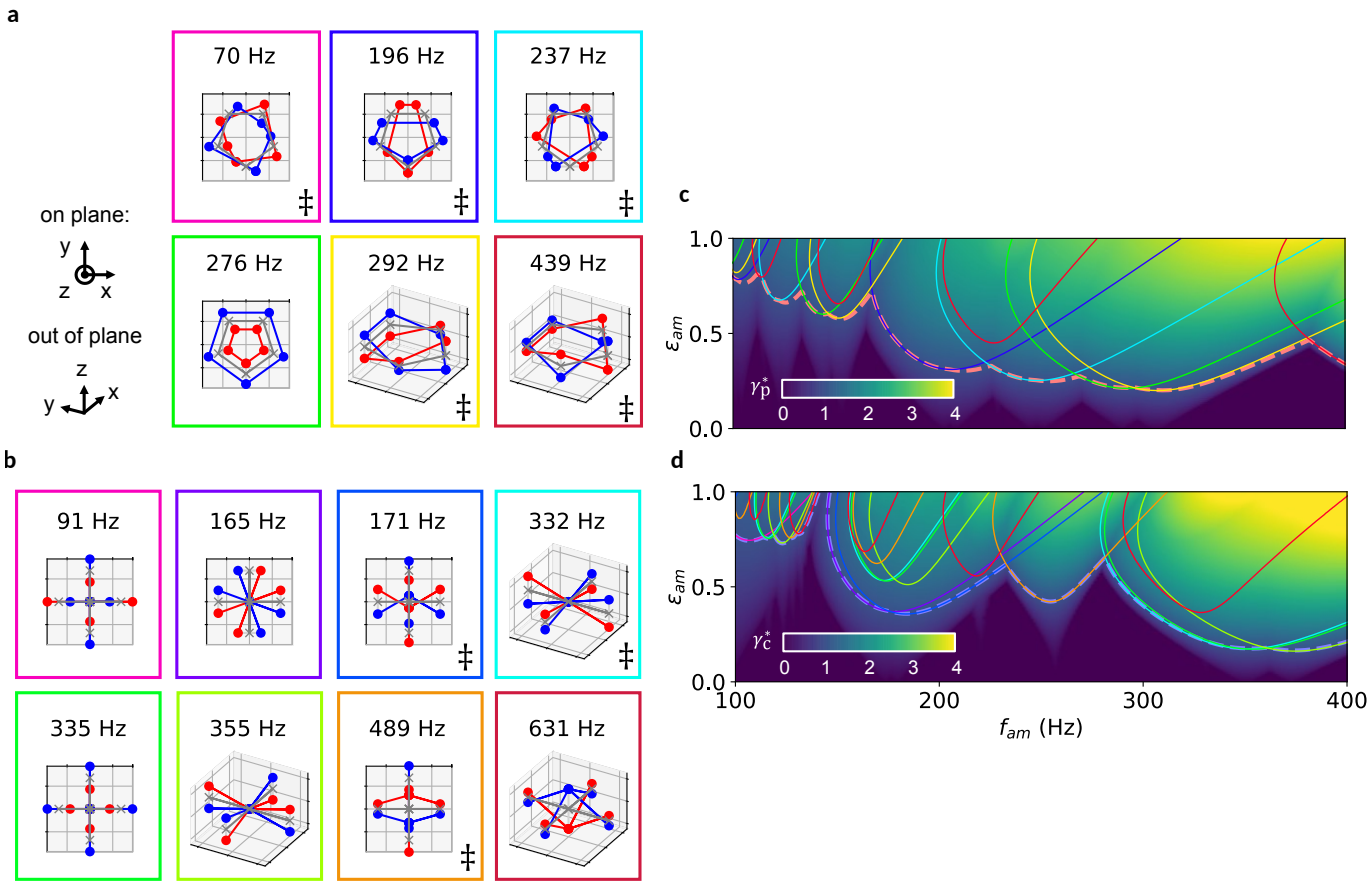

Supplementary Figure 3: Vibrational modes for the two states of the 5-particle cluster. a, All 6 vibrational modes for the pentagon state. **b**, All 8 vibrational modes for the cross state. Maximum and minimum excursions of the particles during each oscillation are shown in blue and red. Degenerate modes are indicated by a double dagger sign. **c-d**, Pumping state diagrams for the pentagon (**c**) and cross (**d**) states. Each mode's contribution to the overall growth rate is marked separately by a line whose color corresponds to the color of the frame around that mode in **a-b**.

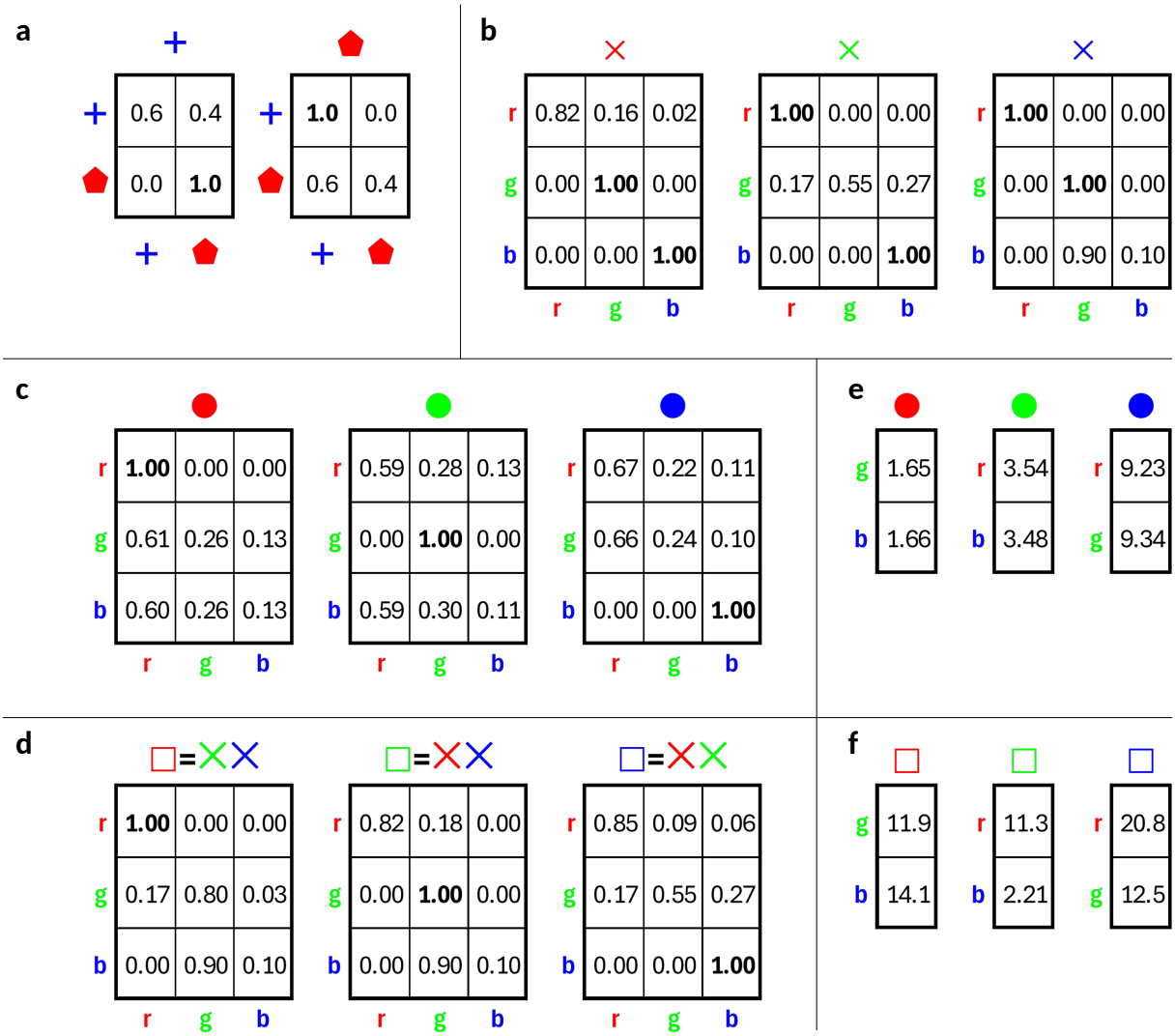

Supplementary Figure 4: Markov models. a, Transition matrices for the levitated 5-particle system when pumped with parameters corresponding to the locations marked by a cross or pentagon in Fig. 3d. **b-f** Simulated system consisting of one rod and two spheres. **b & c** Matrices for transitions between red (r), green (g), and blue (b) states when pumped with parameters marked by crosses and circles in the pumping state diagram, Fig. 4a. **d**, Transition matrices when pumping successively with two sets of parameters indicated by the color of the crosses. These give the predictions in Fig. 4b. **e-f**, The expected quenching steps needed before absorption to the desired state calculated with the Markov model for the simulation system with one rod and two spheres.

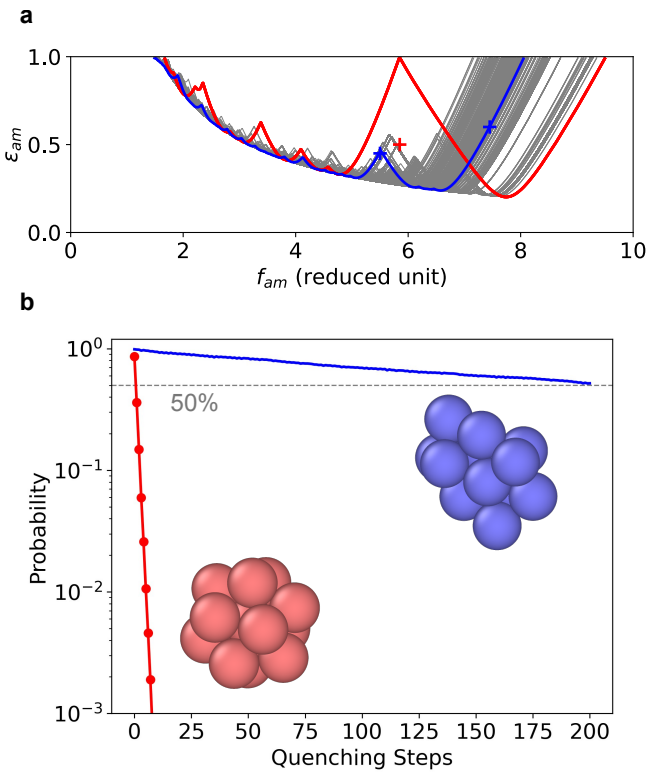

Supplementary Figure 5: Pumping state diagram for a harder-to-select state in the 13-sphere LJ system. a, Pumping state diagrams. The red line shows the boundary above which pumping is possible for the icosahedral sphere arrangement (same as Fig. 4c), and the blue line shows the boundary for a harder-to-select state (shown in blue in panel b). It overlaps more with the boundaries of other structures, making the blue structure harder to select. Gray lines are the boundaries for other structures. The red and blue crosses indicate the parameters used to select each of the two structures. **b**, Probability of not reaching the targeted structure, sketched in red and blue. This probability decreases exponentially for both structures.

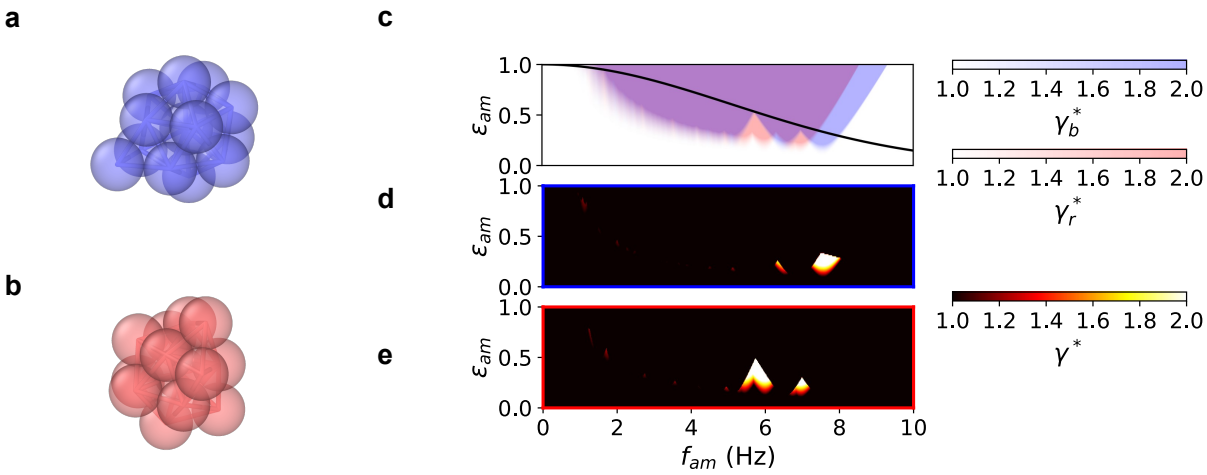

Supplementary Figure 6: Pumping state diagram for the 13-sphere LJ system. a-b, Two different states for $N = 13$. **c**, Pumping state diagrams for the two states. The black line marks the maximum $\varepsilon_{\mathrm{am}}^{\mathrm{eff}}$ as a function of f_{am}. The normalized growth rates γ_b^* and γ_r^* for the blue and red structure are indicated by the corresponding color shading. **d**, Areas in the pumping state diagram where only the blue structure is excited. **e**, Areas in the pumping state diagram where only the red structure is excited. In **d** and **e** areas above the $\varepsilon_{\mathrm{am}}^{\mathrm{eff}}$ line are not included and colors indicate the normalized growth rate γ^*.

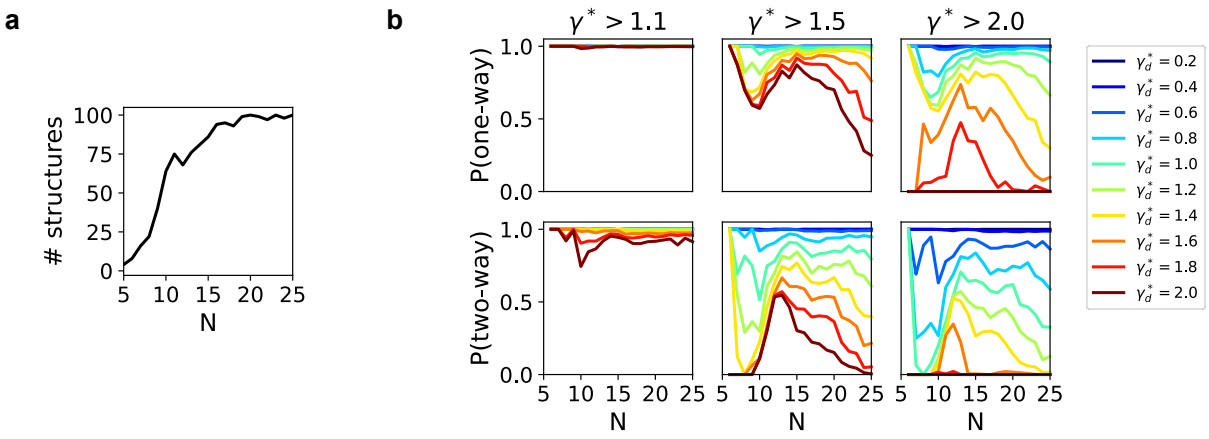

Supplementary Figure 7: Pumping efficiency of the 13-sphere LJ system. **a**, Number of energetically unique structures found out of 100 random trials with N particles. Cluster configuration space rapidly grows with additional particles. **b**. Probability that one-way (top row) and two-way (bottom row) control is possible, given different thresholds for γ^*. One-way control: cluster can transform from one state to the other but not vice versa. Two-way control: cluster can transform between two states. Curves are for a range of damping coefficients γ_d^*, as listed.

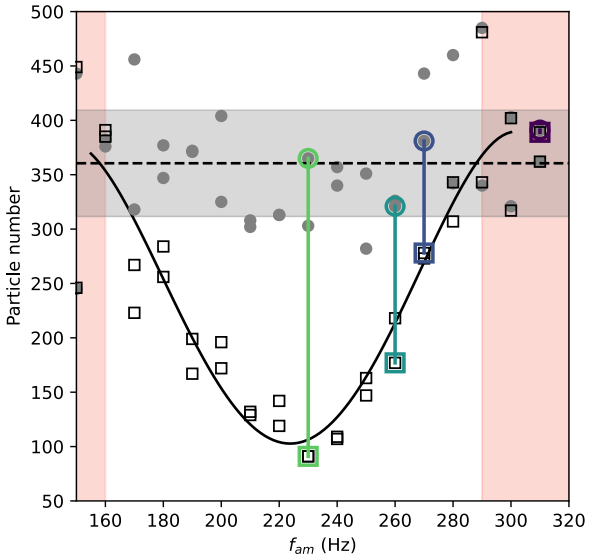

Supplementary Figure 8: Terminal raft size for different f_{am}. Gray circles: initial size of the raft; open black squares: terminal size after 20 pump-quench cycles. The dashed black line gives the averaged initial size across all rafts in this particular set of experiments, and the gray shaded area shows its standard deviation. Pink regions are where no significant size change is observed. In these regions, sometimes the measured terminal size can be slightly larger than initial size, because some particles left outside of the raft at the beginning are not counted, but can rejoin the raft during the pumping process. The black solid line acts as a visual guide, demonstrating the selection of raft size as a function of f_{am}. The four green to purple lines correspond to the rafts in Fig. 5.